PERGAMON

International Journal of Heat and Mass Transfer 45 (2002) 3689–3702

International Journal of HEAT and MASS TRANSFER

www.elsevier.com/locate/ijhmt

Fully coupled solution of a two-phase model for laminar film condensation of vapor–gas mixtures in horizontal channels

E.C. Siow, S.J. Ormiston *, H.M. Soliman

Department of Mechanical and Industrial Engineering, University of Manitoba, Winnipeg, Man., Canada R3T 5V6

Received 30 December 2001; received in revised form 18 February 2002

Abstract

Detailed results are presented for laminar film condensation of vapor–gas mixtures in horizontal flat-plate channels using a fully coupled implicit numerical approach that achieves excellent convergence behavior. These results correspond to steam–air and R134a–air mixtures over wide ranges of the independent parameters, and they include velocity, temperature, and gas concentration profiles, as well as axial variations of film thickness, pressure gradient and Nusselt number. Effects of the four independent variables (inlet values of gas concentration, Reynolds number and pressure, and the inlet-to-wall temperature difference) on the film thickness, pressure gradient, and the local and average Nusselt numbers are carefully examined. It was found that the condensation of R134a–air corresponds to thicker liquid films, lower heat transfer rates, and lower algebraic values of the pressure gradient when compared with steam–air at the same operating conditions.

1. Introduction

Condensation of vapors on cooled surfaces is a very important process due to its fundamental nature, as well as its relevance to many industrial applications. Numerous studies were required in order to develop our current understanding of the physical phenomena involved in the different categories of this process. These categories include, but are not limited to, drop-wise and film condensation; laminar, wavy, and turbulent films; condensation on the exterior of surfaces and inside ducts or channels; condensation of pure vapors, mixtures of vapors, and vapor–gas mixtures. For reviews of condensation heat transfer, the reader is referred to Butterworth et al. [1], Marto [2], Collier and Thome [3], and Rose [4,5].

For internal-flow condensation, most of the published research efforts were concerned with the geometry of a circular tube due to its obvious relevance to many practical applications. The more recent investigations of in-tube condensation were concerned with the effects of the presence of non-condensable gases on the condensation process (e.g. [6–8]). The complexity of the problem did not allow full analytical treatment of the physics involved and therefore, several simplifying assumptions had to be introduced in these investigations, such as using cross-sectionally averaged, one-dimensional conservation equations with empirically based closure relations. This approach may succeed in predicting overall parameters, such as Nusselt number and the condensation rate. However, important features such as the local distributions of velocity, temperature, void, gas concentration, shear stress, and heat flux cannot be predicted unless the full form of the governing conservation equations is considered in the solution.

Our main objective is to investigate the effects of the presence of a non-condensable gas on the process of internal-flow, laminar film condensation using the full form of the governing conservation equations. To the best of our knowledge, there are no results of this type currently available in the literature, with the exception of the work of Yuann et al. [9] on the condensation of vapor–gas mixtures inside vertical tubes. As a start for

* Corresponding author. Tel.: +1-204-474-8639; fax: +1-204-275-7507.

E-mail address: sj_ormiston@umanitoba.ca (S.J. Ormiston).

0017-9310/02/$ - see front matter
PII: S0017-9310(02)00094-7

Nomenclature

C_p	specific heat (J kg^{-1} K^{-1})
D	diffusion coefficient (m^2 s^{-1})
e	relative error, defined in Eq. (26)
H	channel height (m)
h_{fg}	latent heat of vaporization (J kg^{-1})
h_x	local heat transfer coefficient (W m^{-2} K^{-1}) ($= q_x/\Delta T$)
J	mass flow rate at η-direction control volume faces (kg s^{-1})
J''	mass flux at η-direction control volume faces (kg m^{-2} s^{-1})
Ja	Jakob number ($= C_{p,L}(T_{in} - T_{wall})/h_{fg}$)
k	thermal conductivity (W m^{-1} K^{-1})
$\dot{m}$	total mass flow rate (kg s^{-1})
nl	number of grid subdivisions in the η-direction within the liquid film
nv	number of grid subdivisions in the η-direction within the mixture
nx	number of grid subdivisions in the χ-direction
Nu_x	local Nusselt number ($= h_x H/k_L$)
$\overline{Nu_x}$	average Nusselt number ($= (1/x^*)\int_0^{x^*} Nu_x \, dx^*$)
P	pressure (N m^{-2})
P^*	dimensionless pressure ($= (P - P_{in})/(1/2\rho_{in} u_{in}^2)$)
Pr	Prandtl number ($= \mu C_p/k$)
q_x	local heat flux at the lower plate (W m^{-2}) ($= k_L(\partial T_L/\partial y)\|_{y=0}$)
Re_{in}	inlet Reynolds number ($= \rho_{in} u_{in} H/\mu_{in}$)
Re_δ	film Reynolds number ($= (4/\mu_L)\int_0^1 \rho_L u_L \delta \, d\eta$)
Sc	Schmidt number ($= \rho D/\mu$)
T	temperature (K)
ΔT	inlet-to-wall temperature difference (K) ($= (T_{in} - T_{wall})$)
T^*	dimensionless temperature ($= (T - T_{wall})/(T_{in} - T_{wall})$)
u	velocity in the x-direction (m s^{-1})
u^*	dimensionless velocity in the x-direction ($= u/u_{in}$)
v	velocity in the y-direction (m s^{-1})
v^*	dimensionless velocity in the y-direction ($= v/u_{in}$)
W	gas mass fraction
x	coordinate parallel to the channel walls (m)
x^*	dimensionless coordinate parallel to the channel walls ($= x/H$)
y	coordinate normal to the channel walls (m)
y^*	dimensionless coordinate normal to the channel walls ($= y/H$)

Greek symbols

δ	thickness of condensate layer (m)
δ^*	dimensionless film thickness ($= \delta/H$)
η	transformed coordinate defined by Eqs. (23) and (24)
λ	relaxation factor used in Eq. (25)
μ	viscosity (N s m^{-2})
ρ	density (kg m^{-3})
χ	transformed coordinate defined by Eq. (22)

Subscripts

ec	end of condensation path
g	gas
i	interface
in	channel inlet
L	liquid
M	vapor–gas mixture
sat	saturated condition
v	vapor
wall	wall

our research program on this topic, we have selected the geometry of parallel-plate channels, and we plan to extend our work to other duct geometries in the future. The reasons for selecting this geometry are: (a) this geometry is relevant to some practical applications (e.g., plate-fin compact heat exchangers, and cooling systems for the containment buildings of nuclear reactors), (b) the flow can be treated as a two-dimensional problem, which is easier to solve than the three-dimensional formulation required for horizontal and inclined tubes, (c) the present two-dimensional formulation can be easily extended to the case of flow inside vertical tubes, and (d) there are no results available yet for laminar film condensation of vapor–gas mixtures inside channels.

Previous studies on laminar film condensation inside flat-plate channels considered only the case of pure vapors [10–14]. Narain and co-workers [10,11] adopted a one-dimensional, differential–integral formulation of the governing equations, neglected the inertia forces and energy convection in the liquid, assumed a constant temperature in the vapor, and imposed an assumed formulation for the shear stress at the interface and the upper wall. Louahlia and Panday [12–14] followed a more-accurate, two-dimensional approach in which they retained the liquid inertia and convection terms, and imposed continuity of shear stress and heat flux at the vapor–liquid interface. The governing conservation equations, which were developed for both phases, were

solved numerically using a segregated solution method, whereby each of the governing non-linear equations was iterated separately until convergence was achieved for the whole system at each axial cross-section.

The model developed in the present work includes the complete two-dimensional, two-phase, boundary-layer equations for laminar film condensation of vapor–gas mixtures inside channels. Numerical solution of this model has been achieved using a fully coupled approach, whereby the whole system of non-linear governing equations was iterated simultaneously at each axial cross-section until convergence was achieved. This approach makes the solution scheme robust by mitigating solution oscillations caused by inter-equation coupling and also avoids the numerous under-relaxation factors that may be required for a segregated method. Also, this approach was found to produce excellent convergence behavior, even in the cases of high inlet gas concentrations. This paper presents the numerical model used and detailed original results on laminar film condensation in horizontal channels in the presence of a non-condensable gas.

2. Mathematical model

The geometry under consideration is shown in Fig. 1. A mixture of a saturated vapor and a non-condensable gas (total mass flow rate $\dot{m}_{\text{in}}$) enters a horizontal, parallel-plate channel of height H with a top wall that is insulated and a bottom wall that is is cooled and maintained at a uniform temperature T_{wall}. The mixture enters with a uniform velocity u_{in}, uniform temperature T_{in}, uniform pressure P_{in}, and uniform gas concentration W_{in}. As the mixture flows down the channel, vapor is removed from the mixture to form a condensate layer of thickness δ on the bottom plate. Hydrodynamic, thermal, and concentration boundary layers build within the mixture layer along the upper wall and the liquid–mixture interface. Along the condensation path (i.e., in the x-direction), there is a continuous change in the velocity and temperature profiles in the liquid and mixture layers, the gas-concentration profile in the mixture, the pressure and the axial pressure gradient, the film thickness, and the local heat transfer coefficient at the lower wall.

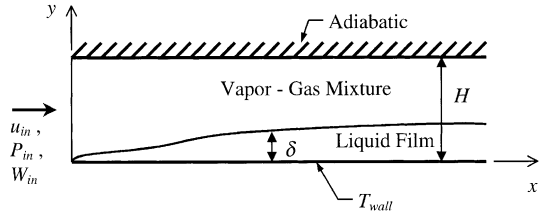

Fig. 1. Geometry and coordinate system.

In formulating the governing conservation equations, it was assumed that the flow is steady and laminar, the liquid–mixture interface is smooth, and the liquid and mixture are Newtonian fluids. The vapor–gas mixture was treated as an ideal-gas mixture and saturation conditions were assumed at the liquid–mixture interface. The pressure, P, was assumed to be constant across the channel (i.e., $\partial P/\partial y = 0$); however, P varies in the x-direction due to frictional losses and momentum change. Finally, the axial diffusion of heat, momentum, and mass were assumed to be negligible.

The governing equations, written in the Cartesian coordinates shown in Fig. 1, are:

$$\frac{\partial}{\partial x}(\rho_{\text{L}} u_{\text{L}}) + \frac{\partial}{\partial y}(\rho_{\text{L}} v_{\text{L}}) = 0, \tag{1}$$

$$\frac{\partial}{\partial x}(\rho_{\text{L}} u_{\text{L}} u_{\text{L}}) + \frac{\partial}{\partial y}(\rho_{\text{L}} v_{\text{L}} u_{\text{L}}) = \frac{\partial}{\partial y}\left(\mu_{\text{L}} \frac{\partial u_{\text{L}}}{\partial y}\right) - \frac{\mathrm{d}P}{\mathrm{d}x}, \tag{2}$$

$$\frac{\partial}{\partial x}\left(\rho_{\text{L}} u_{\text{L}} C_{\text{p,L}} T_{\text{L}}\right) + \frac{\partial}{\partial y}\left(\rho_{\text{L}} v_{\text{L}} C_{\text{p,L}} T_{\text{L}}\right) = \frac{\partial}{\partial y}\left(k_{\text{L}} \frac{\partial T_{\text{L}}}{\partial y}\right), \tag{3}$$

$$\frac{\partial}{\partial x}(\rho_{\text{M}} u_{\text{M}}) + \frac{\partial}{\partial y}(\rho_{\text{M}} v_{\text{M}}) = 0, \tag{4}$$

$$\frac{\partial}{\partial x}(\rho_{\text{M}} u_{\text{M}} u_{\text{M}}) + \frac{\partial}{\partial y}(\rho_{\text{M}} v_{\text{M}} u_{\text{M}}) = \frac{\partial}{\partial y}\left(\mu_{\text{M}} \frac{\partial u_{\text{M}}}{\partial y}\right) - \frac{\mathrm{d}P}{\mathrm{d}x}, \tag{5}$$

$$\frac{\partial}{\partial x}(\rho_{\text{M}} u_{\text{M}} C_{\text{p,M}} T_{\text{M}}) + \frac{\partial}{\partial y}(\rho_{\text{M}} v_{\text{M}} C_{\text{p,M}} T_{\text{M}}) = \frac{\partial}{\partial y}\left(k_{\text{M}} \frac{\partial T_{\text{M}}}{\partial y}\right) + \frac{\partial}{\partial y}\left[\rho_{\text{M}} D\left(C_{\text{p,g}} - C_{\text{p,v}}\right) \frac{\partial W}{\partial y} T_{\text{M}}\right], \tag{6}$$

$$\frac{\partial}{\partial x}(\rho_{\text{M}} u_{\text{M}} W) + \frac{\partial}{\partial y}(\rho_{\text{M}} v_{\text{M}} W) = \frac{\partial}{\partial y}\left(\rho_{\text{M}} D \frac{\partial W}{\partial y}\right). \tag{7}$$

Eqs. (1)–(3) govern the conservation of mass, momentum, and energy for the liquid film, while Eqs. (4)–(6) are the corresponding conservation equations for the mixture. Eq. (7) ensures mass conservation for the gas. Thermal and mechanical equilibria have been assumed in the mixture, i.e., the vapor and the gas are assumed to have the same values of u, v, and T at any location within the mixture. In solving the above set of governing equations, the properties were calculated as functions of the local pressure, temperature, and mixture composition, as described in [15].

The boundary conditions for Eqs. (1)–(7) are:

- Lower plate ($y = 0$)

$$u_{\text{L}} = 0, \tag{8}$$

$$v_{\text{L}} = 0, \tag{9}$$

$$T_{\text{L}} = T_{\text{wall}}. \tag{10}$$

- Upper plate ($y = H$)

$$u_M = 0, \tag{11}$$

$$v_M = 0, \tag{12}$$

$$\frac{\partial T_M}{\partial y} = 0, \tag{13}$$

$$\frac{\partial W}{\partial y} = 0. \tag{14}$$

- Liquid–mixture interface ($y = \delta$)

$$u_L = u_M, \tag{15}$$

$$\mu_L \frac{\partial u_L}{\partial y} = \mu_M \frac{\partial u_M}{\partial y}, \tag{16}$$

$$\rho_L v_L - \rho_L u_L \frac{d\delta}{dx} = \rho_M v_M - \rho_M u_M \frac{d\delta}{dx} = J_i'', \tag{17}$$

$$T_L = T_M = T_{sat,i}, \tag{18}$$

$$J_i'' W - \rho_M D \frac{\partial W}{\partial y} = 0. \tag{19}$$

$$k_L \frac{\partial T_L}{\partial y} = k_M \frac{\partial T_M}{\partial y} - J_i'' h_{fg}. \tag{20}$$

The above boundary conditions prescribe no slip on the isothermal (lower) plate, no slip and gas impermeability at the insulated (upper) plate, continuity of velocity and shear stress at the interface, as well as mass and energy balances and gas impermeability at the interface.

The system of governing equations (1)–(7), along with boundary conditions (8)–(20) provide the necessary relations for determining the field variables u_L, v_L, T_L, u_M, v_M, T_M, W, and δ. An additional relation is required for determining the local pressure gradient, dP/dx, along the channel. This was achieved by invoking overall mass conservation:

$$\int_0^\delta \rho_L u_L \, dy + \int_\delta^H \rho_M u_M \, dy = \dot{m}_{in}. \tag{21}$$

For a specified vapor–gas mixture at the inlet of the channel, the required input values for solving the above model are u_{in} (or $\dot{m}_{in}$), T_{in} (or P_{in}), W_{in}, and T_{wall} (or ΔT).

Far downstream from the inlet, the temperature across the condensate and the mixture layers cools down to T_{wall} and the condensation process shuts off. The mixture composition at this location reduces to a gas fully saturated with vapor. The gas concentration in this mixture, W_{ec}, can be easily determined from the local pressure, P_{ec}, the local temperature, T_{wall}, and the properties of gas and vapor [16]. This flow situation is easy to solve and a summary of the procedure and results is presented in Appendix A.

3. Numerical solution method

In an approach similar to that of Chin et al. [17], a transformation of coordinates is made before discretization of the governing equations to enable the use of a computational grid in which the liquid–mixture interface is clearly defined at all stations along the solution domain. In this work, the Cartesian x–y coordinates are transformed into χ–η coordinates using [18]:

$$\chi = x \quad \text{for all } x, \tag{22}$$

$$\eta = \frac{y}{\delta} \quad \text{for } 0 \leqslant y \leqslant \delta, \tag{23}$$

$$\eta = \frac{y - \delta}{H - \delta} + 1 \quad \text{for } \delta \leqslant y \leqslant H. \tag{24}$$

The solution domain was then divided into transformed coordinates into control volumes in a structured grid. A finite volume method [19] was applied to the transformed equations resulting in a set of non-linear algebraic equations for the seven nodal unknowns u_L, J_L, T_L, u_M, J_M, T_M, and W and for the scalar unknowns δ and $dP/d\chi$ at each axial station. It was more convenient in the numerical solution method to use mass flow J in place of the v velocity in the solution fields. Standard upwind approximations were used for the control-volume face values in the χ-direction, an algebraic approximation for the Exponential Differencing Scheme was used for the control-volume face values in the η-direction, and non-linear and inter-equation coupling terms were approximated using a Newton–Raphson linearization [18]. The boundary conditions were prescribed using zero-width control volumes at each plate and at the liquid–mixture interface.

A marching procedure was used in the numerical solution. The inlet boundary condition was used as an initial guess to form the linearized coupled equations for the first χ station (column of control volumes in the liquid and mixture). The linearized equation set was solved directly using a bordered-matrix algorithm and a block TDMA [18]. The direct solution of the linearized equations was repeated with an update of all coefficients in each iteration. Relaxation was applied at all the nodal points for the solution fields and the two scalars. The relaxation method can be represented by

$$\phi^{new} = \phi^k + \lambda(\phi^{k+1} - \phi^k), \tag{25}$$

where k is the iteration index and ϕ represents a solution field variable. Typical relaxation factors used were 0.4 for the film thickness, 0.8 for the temperature, and no relaxation for all other unknowns. Convergence of the solution at a station was determined using relative error assessment. The relative error e, was calculated as

$$e = \left| \frac{\phi^{k+1} - \phi^k}{\phi^{k+1}} \right|. \tag{26}$$

Convergence was declared at a station when e was less than 1×10^{-7} for all field values at all nodal points and for δ and $dP/d\chi$. After a converged solution was obtained at any given axial station, the solution procedure was repeated for the column of control volumes at the next station using the previous-station solution as an initial guess. Computation proceeded station by station along the channel until either the prescribed channel length was reached or one of the following three conditions was encountered:

- Complete condensation was achieved. For pure vapors, this was assumed when $\delta = H$ was reached, and for vapor–gas mixtures, this was assumed when the field values approached closely those given in Appendix A.
- Flow reversal (i.e., negative values of u) was encountered. Whenever this condition was encountered, it was always located near the upper wall of the channel and it coincided with high values of ΔT and low values of W_{in}. The solution cannot be progressed beyond this cross-section because of the parabolic solution method adopted in this investigation.
- The film Reynolds number, Re_δ, exceeded 30. This condition was never invoked for any of the conditions considered in this investigation.

The numerical solution described above was implemented in a new, in-house computer code. The computer code was tested thoroughly for consistency and accuracy by means of local and overall conservation balance checks, grid independence tests, and validation tests. Grid independence tests were carried out by comparing the total heat transfer to the bottom plate for different values of nl, nv, and nx for a channel of fixed dimensions (height 2 cm and length 8 m). The range of values considered was as follows: $10 \leqslant nl \leqslant 40$, $40 \leqslant nv \leqslant 160$, and $100 \leqslant nx \leqslant 400$. In all cases, the grid in the liquid region was uniformly spaced in the η-direction, the grid in the mixture region was contracted geometrically toward the upper plate and toward the liquid–mixture interface in the η-direction, and the grid expanded exponentially along χ after a short section (0.005 m long) with five uniformly spaced stations adjacent to the inlet. It was found that a grid with $nl = 40$, $nv = 80$, and $nx = 200$ produced results for total heat transfer that were less than 0.1% different from those obtained using the finest grid [18]. All the results presented in Section 4 were generated using this mesh, and therefore we can claim less than 1% in numerical uncertainty.

Two validation tests were performed against previously published results (experimental and theoretical). The first validation test was for condensation of pure saturated refrigerant R-113 flowing in a nominally horizontal parallel-plate channel. A comparison was made for $\delta(x)$ between the present work, the experimental results of Lu and Suryanarayana [20], and the numerical results of Louahlia and Panday [12]. In the second validation test, the results from the present model were compared with those from an earlier in-house code that used a segregated numerical approach to compute external-flow, laminar film condensation on isothermal plates with a non-condensable gas [17]. In order to perform this comparison, a flat-plate channel with a relatively large height and a relatively small length, was used in the present model. In both the validation tests, good agreement was found [18]. The second validation test also indicated that the present method has much better convergence behavior than a segregated method, especially for high inlet gas concentration values.

The variable transformation used in [15,17] was applied to Eqs. (1)–(7). As a result, the following dimensionless groups were identified: $x^*, y^*, \delta^*, u^*, v^*$, Re_{in}, P^*, T^*, Ja, Sc, and Pr. The other dimensionless groups that resulted from this transformation are $(T_{wall}/\Delta T)$ and the property ratios (ρ_L/ρ_M), (μ_L/μ_M), (k_L/k_M), and $(C_{p,g} - C_{p,v})/C_{p,M}$. The dimensionless coordinate y^* is related to the transformed coordinate η by the following relations:

$$\eta = y^*/\delta^* \quad \text{for } 0 \leqslant y^* \leqslant \delta^*, \tag{27}$$

$$\eta = \frac{y^* - \delta^*}{1 - \delta^*} + 1 \quad \text{for } \delta^* \leqslant y^* \leqslant 1. \tag{28}$$

The transformed conservation equations and boundary conditions indicated that the four field variables u^*, v^*, T^*, and W are functions of $x^*, y^*, W_{in}, Re_{in}$, $(T_{wall}/\Delta T)$, and the fluid properties. If the vapor–gas combination is specified along with values of P_{in}, W_{in}, and ΔT, then it is possible to calculate T_{in} and T_{wall}. Thus, during the computations, the local values of T were available for calculating the properties. Therefore, for a known vapor–gas composition, values of $W_{in}, \Delta T, Re_{in}$, and P_{in} are the only required input for the calculation of u^*, v^*, T^*, and W as functions of x^* and y^*. The validity of this dependence was confirmed numerically by generating results at the same Re_{in} but different combinations of u_{in} and H and observing that the results would collapse. The calculated field parameters were used in determining some important engineering parameters, such as the local and the average Nusselt numbers, Nu_x and $\overline{Nu_x}$, respectively, as defined in the nomenclature.

4. Results and discussion

Two vapor–gas combinations (steam–air, and R134a–air) were considered in this investigation. Steam and air are two of the most commonly used fluids in practice, and R134a is one of the new fluids developed for refrigeration applications. Also, these two combinations include a mixture of a vapor and a heavier gas

(steam–air) and a mixture of a vapor and a lighter gas (R134a–air).

4.1. Results for steam–air mixtures

For the vapor–gas combination of steam–air, results were obtained for three inlet pressures ($P_{in} = 0.5$, 1, and 2 atm), four inlet-to-wall temperature differences ($\Delta T =$ 5, 10, 20, and 50 K), three inlet Reynolds numbers ($Re_{in} = 500$, 1000, and 2000), and a range of inlet gas concentrations ($0 \leqslant W_{in} \leqslant 0.2$). The results presented here include the detailed profiles of velocity, temperature, and gas concentration, as well as the variations of film thickness, Nusselt number, and pressure along the condensation path.

4.1.1. Common behavior

The results obtained in this investigation were found to follow a common behavior for all inlet conditions. This behavior is illustrated in the six parts of Fig. 2, which corresponds to steam–air at the inlet conditions of $Re_{in} = 2000$, $P_{in} = 1$ atm, $W_{in} = 0.1$, and $\Delta T = 20$ K.

Fig. 2(a) shows the axial-velocity profiles plotted in terms of u^* versus η at different values of x^* (please note that different vertical scales are used in the liquid, $0 \leqslant \eta \leqslant 1$, and the mixture, $1 \leqslant \eta \leqslant 2$, regions). In the early segment of the condensation path (e.g., at $x^* = 5$), boundary layers can be seen to form in the mixture region at the liquid–mixture interface and the upper wall, while a uniform value of u^*_M (slightly greater than one) still persists in the core. Further along the condensation

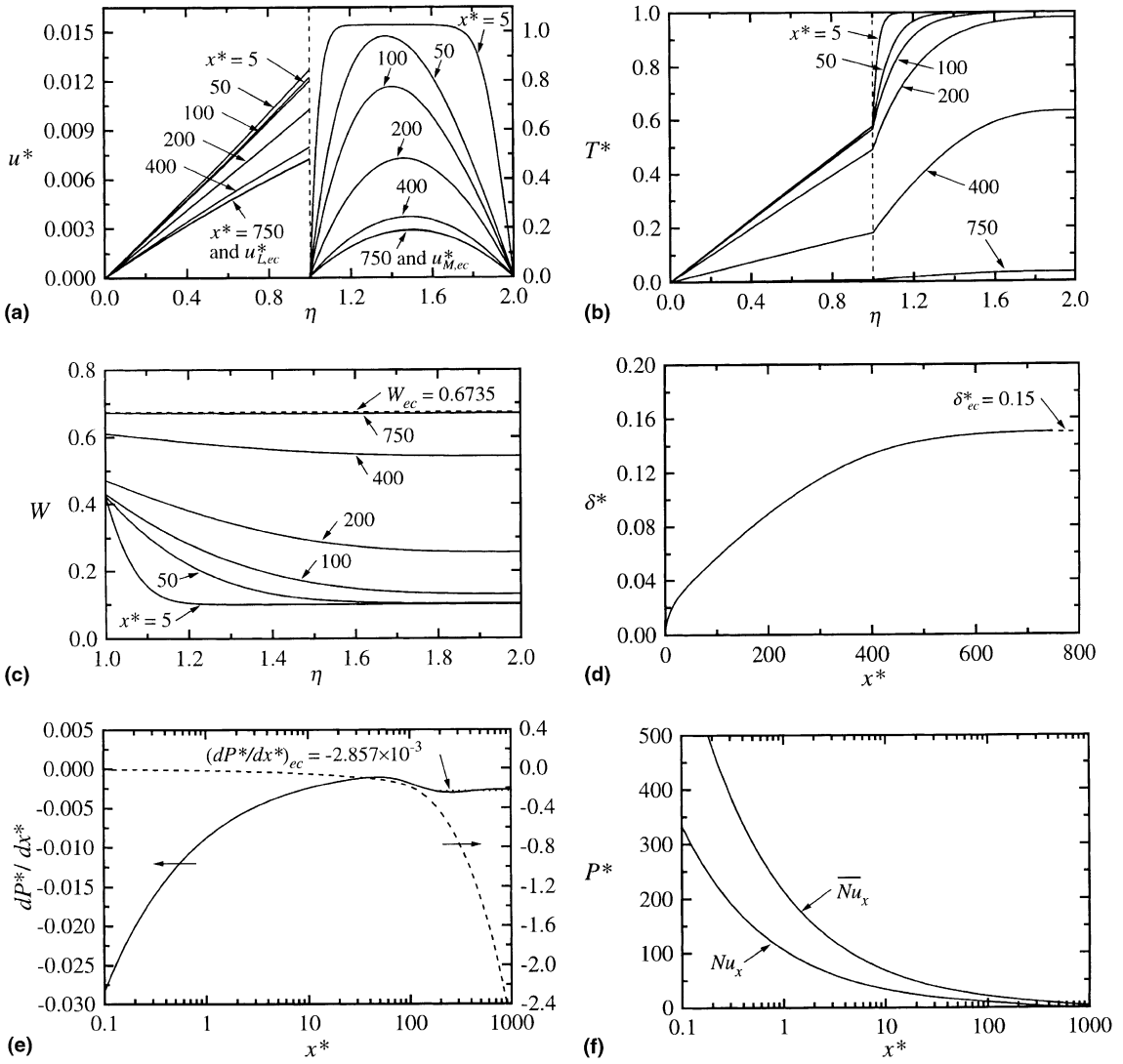

Fig. 2. Results for steam–air at $P_{in} = 1$ atm, $Re_{in} = 2000$, $W_{in} = 0.1$, and $\Delta T = 20$ K; (a) velocity profiles; (b) temperature profiles; (c) gas concentration profiles; (d) film thickness; (e) pressure and pressure gradient; (f) local and mean Nusselt numbers.

path, both boundary layers get thicker and the mean velocity of the mixture decreases due to the loss of mass associated with the condensation process. At a large distance from the inlet (e.g., $x^* = 750$ for the values of Re_{in}, P_{in}, W_{in}, and ΔT used in Fig. 2), the condensation process practically shuts off. The mixture at this location consists of air fully saturated with water vapor at $T_M \cong T_{wall}$, and the velocity profile converges closely to the exact solution $u^*_{M,ec}$ presented in Appendix A. In the liquid film, the velocity profiles presented in Fig. 2(a), show that values of u^*_L are relatively high at the beginning of the condensation path, where the condensate mass flow rate is small and the drag force from the mixture is high. After a slight increase at $x^* = 50$, values of u^*_L decrease along the condensation path due to the decreasing interfacial drag and the increasing film thickness. Again, at $x^* = 750$, the u^*_L profile converges closely to the $u^*_{L,ec}$ profile of Appendix A.

Fig. 2(b) shows the profiles of T^* in the liquid and mixture regions at various axial locations. The temperature level across both regions decreases continuously in the flow direction. The T^*_L profiles are fairly close to a linear shape, which indicates that the convection terms in the liquid energy equation are not very significant. The mixture temperature T_M starts out at T_{sat} at $x = 0$ and appears to approach T_{wall} at large values of x. The slope $(\partial T^*_L/\partial \eta)$ at the interface decreases continuously along x^*, which indicates a decreasing rate of heat transfer along the condensation path.

The profiles of the gas concentration W are shown in Fig. 2(c). A uniform profile, $W = W_{in} = 0.1$, was assumed at the inlet ($x^* = 0$). It is clear from Fig. 2(c) that in the early part of the condensation path, W increases very rapidly near the interface (e.g., at the interface, $W_i > 0.4$ at $x^* = 5$) with a high value of $(\partial W/\partial y)_i$ for $x^* > 5$, W rises continuously at all η locations, while $(\partial W/\partial y)_i$ decreases continuously until the end of the condensation process is approached (e.g., at $x^* = 750$), where a fairly flat W profile is reached. The flat W profile at $x^* = 750$ is very close to the value of $W_{ec} = 0.6735$ that corresponds to air fully saturated with water vapor at $T_M = T_{wall}$ and the local pressure.

The development of the liquid film thickness along x^* is illustrated in Fig. 2(d). For this value of W_{in}, the value of δ^*, increases continuously with x^* while $\partial\delta^*/\partial x^*$ decreases continuously with x^*. This trend of decreasing $\partial\delta^*/\partial x^*$ is typical of results for larger W_{in} and is consistent with the trends seen earlier of increasing W_i (which results in decreasing T_i), increasing film thickness, and therefore decreasing $(\partial T_L/\partial y)_i$ and interfacial heat flux.

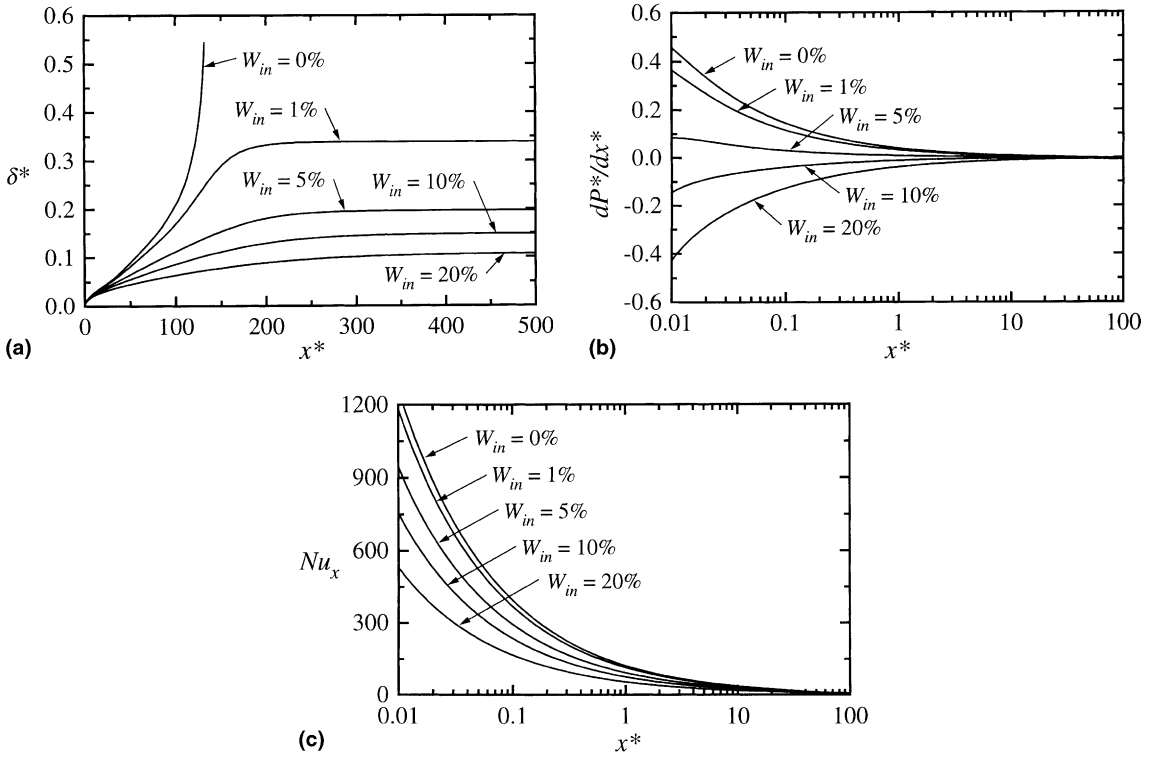

Fig. 3. Effect of W_{in} on the results of steam–air at $P_{in} = 1$ atm, $Re_{in} = 1000$, and $\Delta T = 20$ K; (a) liquid film thickness; (b) pressure gradient; (c) local Nusselt number.

At $x^* = 750$, the present numerical solution converges very closely to the algebraic solution (Appendix A) of $\delta^*_{ec} = 0.15$.

The axial variations of P^* and $(\partial P^*/\partial x^*)$ are shown in Fig. 2(e). The pressure gradient $(\partial P^*/\partial x^*)$ is the sum of two components; a positive component due to the loss of momentum associated with the condensation process and a negative component due to friction at both walls of the channel. The algebraic sum of these two components is negative at all x^* for the flow conditions corresponding to Fig. 2(e) and therefore, the pressure decreases continuously from inlet to exit. At the end of the condensation path, the momentum component disappears and the frictional component becomes invariant along x^*. The analytical solution in Appendix A gives $(dP^*/dx^*)_{ec} = -0.002857$ and the numerical solution in Fig. 2(e) appears to approach this value very closely at $x^* = 750$.

The local and the average Nusselt numbers at the lower plate Nu_x and $\overline{Nu}_x$, respectively, are presented in Fig. 2(f). As expected, Nu_x decreases rapidly along x^* and it approaches zero at $x^* = 750$, which is close to the end of the condensation path. This rapid decrease in Nu_x is caused by the combined effects of a continuous decrease in $(T_i - T_{wall})$ and a continuous increase in δ along x^*. Values of $\overline{Nu}_x$, shown in Fig. 2(f), can be very useful in calculating the overall rate of heat transfer between the channel inlet and any axial location downstream. The magnitude and trend in the results of $\overline{Nu}_x$ versus x^* are consistent with those in the Nu_x versus x^* results.

The above results for steam–air mixtures correspond to a particular combination of the independent variables (Re_{in}, P_{in}, W_{in}, and ΔT). Effects of these independent variables on the values of δ^*, (dP^*/dx^*), and Nu_x are examined in the following sections.

4.1.2. Effect of W_{in}

The influence of W_{in} on the condensation process was examined for steam–air at $Re_{in} = 1000$, $P_{in} = 1$ atm, and $\Delta T = 20$ K. The results shown in Figs. 3(a)–(c) clearly confirm that the presence of gas in the vapor stream has a very strong effect on the condensation process. Fig. 3(a) shows the impact of W_{in} on the thickness of the liquid layer along the condensation path. At any x^*, the film thickness is largest for pure vapors. The presence of gas dictates that the flow channel will never run full of liquid at the end of the condensation path. Fig. 3(a) shows that δ^*_{ec} decreases as W_{in} increases. As well, δ^* and $(\partial\delta^*/\partial x^*)$ decrease at all values of x^* as W_{in} increases, indicating a decreased heat transfer rate. The solution for the pure

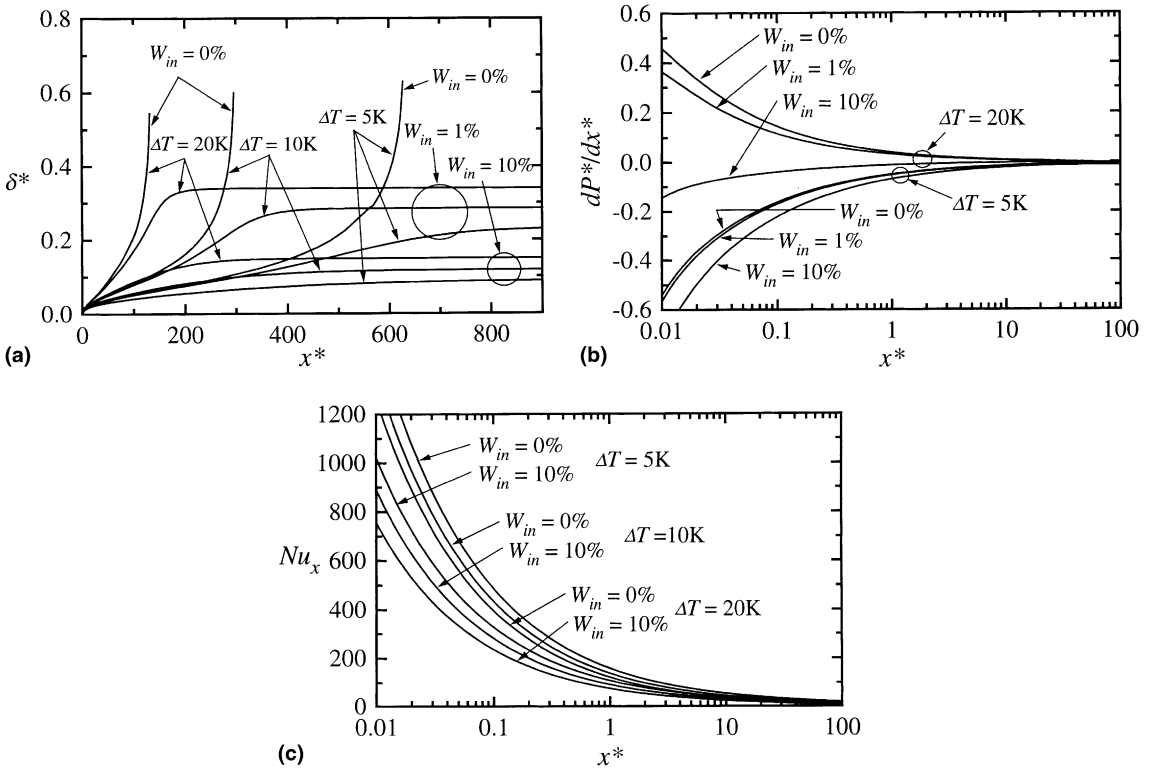

Fig. 4. Effect of ΔT on the results of steam–air at $P_{in} = 1$ atm and $Re_{in} = 1000$; (a) liquid film thickness; (b) pressure gradient; (c) local Nusselt number.

vapor in Fig. 3(a) could not be progressed beyond the point shown in the figure because of flow reversal. However, for all practical purposes, the condensation process was complete when flow reversal occurred as over 99% of the vapor had already been condensed.

The impact of W_{in} on the pressure gradient is also very significant, as shown in Fig. 3(b). For a pure vapor, (dP^*/dx^*) is actually positive for a significant portion of the condensation path and it turns negative only at $x^* \cong 25$. This suggests that the positive momentum component of the pressure gradient is high enough (due to the high condensation rate) for $x^* < 25$ to overcome the negative frictional component. Further along the channel (i.e., $x^* > 25$), both the condensation rate and the momentum component decrease and the net value of (dP^*/dx^*) becomes negative. As W_{in} increases, the momentum component of the pressure gradient decreases due to the decreased condensation rate, which results in an overall decrease in (dP^*/dx^*). For $W_{in} > 0.1$, the results in Fig. 3(b) show that the pressure gradient is negative throughout the condensation path.

Fig. 3(c) shows the impact of the presence of gas on heat transfer. As expected, significant reductions in Nu_x are introduced and the magnitude of these reductions increases as W_{in} increases. At $W_{in} = 0.1$, there is approximately 50% reduction in heat transfer compared to the values for pure vapor. For all values of W_{in}, Nu_x approaches zero at large x^*.

4.1.3. Effect of ΔT

The effect of ΔT on the condensation parameters was investigated for steam–air at $Re_{in} = 1000$, $P_{in} = 1$ atm, and different values of W_{in} and the results are shown in Figs. 4(a)–(c). For fixed values of P_{in} and W_{in}, the inlet saturation temperature will be fixed and therefore, increasing ΔT means decreasing T_{wall}. At the end of the condensation path where the liquid and mixture temperatures reduce to T_{wall}, an increase in ΔT would then mean a reduced ability for the gas to absorb moisture, i.e., a decrease in W_{ec} (because of the decrease in T_{wall}). Consequently, an increase in ΔT at fixed P_{in}, W_{in}, and Re_{in} would result in an increase in the mass flow rate of the liquid condensate at the end of the condensation path.

Fig. 4(a) shows the effect of ΔT on δ^* at $W_{in} = 0$, 0.01, and 0.1. For pure steam, a significant increase in $(\partial\delta^*/\partial x^*)$ and a significant decrease in the channel length required for complete condensation can be seen as ΔT increases. These trends suggest that an increase in heat flux is associated with the increase in ΔT. Similar trends can be seen in Fig. 4(a) with air present, i.e., increasing $(\partial\delta^*/\partial x^*)$ and decreasing condensation length with increasing ΔT. The value of δ^*_{ec} increases as ΔT increases

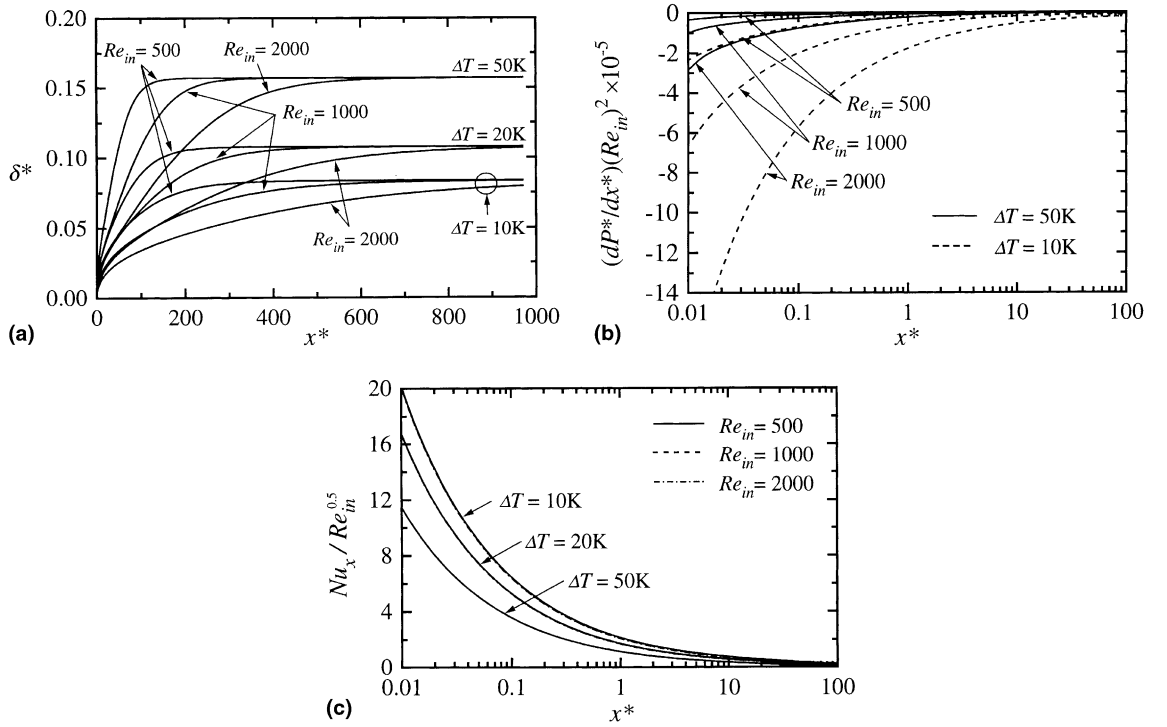

Fig. 5. Effect of Re_{in} on the results of steam–air at $P_{in} = 1$ atm and $W_{in} = 0.2$; (a) liquid film thickness; (b) pressure gradient; (c) local Nusselt number.

because of the increase in the mass flow rate of the liquid condensate, as discussed above.

The effect of ΔT on the axial pressure gradient is illustrated in Fig. 4(b). The trend in these results is that an increase in ΔT or a decrease in W_{in} has similar effects on (dP^*/dx^*). This is attributed to the fact that either an increase in ΔT or a decrease in W_{in} would, according to earlier results, result in an increase in the wall heat flux causing a faster condensation rate and consequently, a larger value for the momentum component of (dP^*/dx^*). In all cases, (dP^*/dx^*) is negative near the end of the condensation path because the momentum component diminishes and the friction component dominates.

Fig. 4(c) shows the effect of ΔT on Nu_x for $W_{in} = 0$ and 10%. These results show that Nu_x decreases at any value of x^* as ΔT increases. A similar trend exists in the classical Nusselt's [21] solution for laminar film condensation of pure vapors on vertical isothermal plates where Nu_x is proportional to $(\Delta T)^{-0.25}$. An attempt to replot the results in Fig. 4(c) in terms of $[Nu_x(\Delta T^a)]$ versus x^* did not succeed in identifying values for the exponent a that would collapse the results for various ΔT at the same W_{in}. Exponent a was found to vary along x^*. In spite of the decrease in Nu_x, the wall heat flux was found to increase with ΔT. For example, for $W_{in} = 0\%$, the overall rate of heat transfer from $x^* = 0$ to $x^* = 103$ increased by about 54% as ΔT was increased from 5 to 10 K, and a further increase of about 40% occurred as ΔT was increased from 10 to 20 K. For $W_{in} = 10\%$, the overall rate of heat transfer from $x^* = 0$ to $x^* = 103$ increased by about 56% as ΔT was increased from 5 to 10 K, and a further increase of about 46% occurred as ΔT was increased from 10 to 20 K.

4.1.4. Effect of Re_{in}

Effect of the inlet Reynolds number on the condensation parameters was investigated for steam–air at $P_{in} = 1$ atm, $W_{in} = 0.2$, and $10 \leqslant \Delta T \leqslant 50$ K. Fig. 5(a) shows the results for δ^*. These data demonstrate that increasing Re_{in} at fixed P_{in}, W_{in}, and ΔT results in increasing the channel length required for complete condensation. However, the thickness of the condensate layer at the end of the condensation path remains unchanged with Re_{in}, consistent with the analytical result in Appendix A. The increase in δ^* with ΔT, seen in Fig. 5(a), was explained in Section 4.1.3.

Fig. 5(b) shows results for the effect of Re_{in} on the axial pressure gradient. Values of $[(dP^*/dx^*)Re_{in}^2]$ were plotted on the vertical axis because this quantity is proportional to the dimensional pressure gradient (dP/dx). Fig. 5(b) shows a significant increase in the absolute value of the pressure gradient with increasing Re_{in}. This trend is expected since the frictional compo-

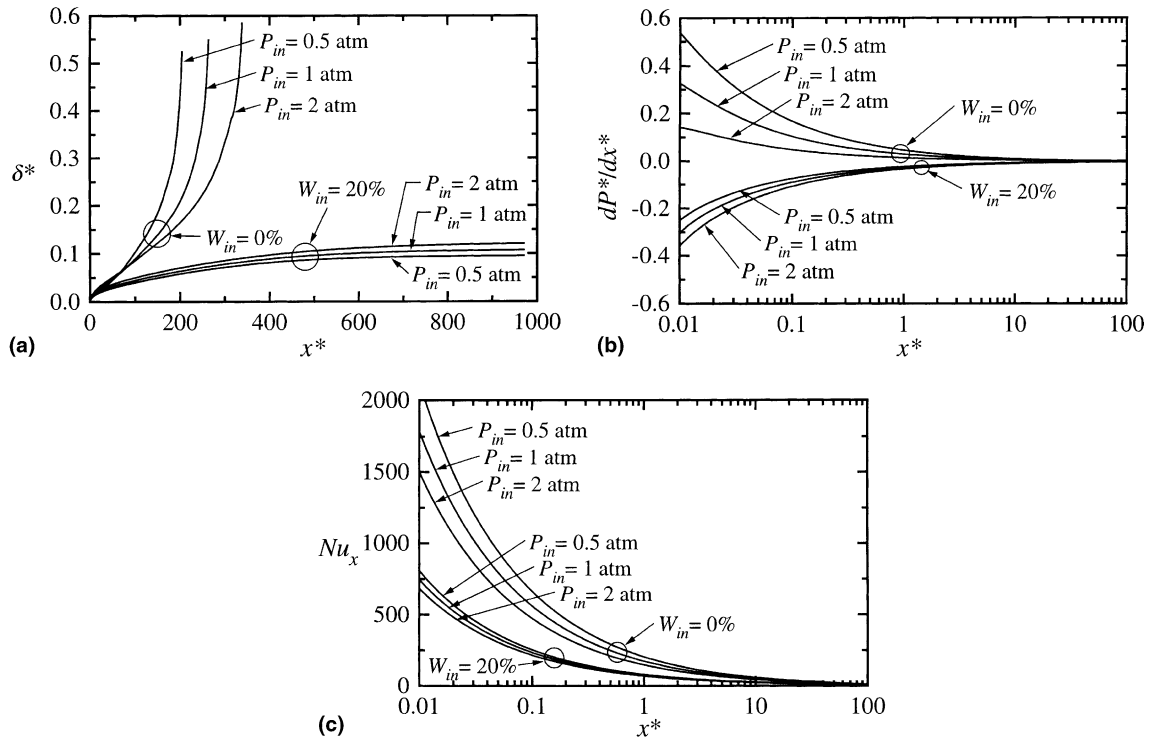

Fig. 6. Effect of P_{in} on the results of steam–air at $Re_{in} = 2000$ and $\Delta T = 20$ K; (a) liquid film thickness; (b) pressure gradient; (c) local Nusselt number.

nent of (dP/dx) would increase significantly as Re_{in} increases.

The effect of Re_{in} on heat transfer is presented in Fig. 5(c) in terms of $(Nu_x/Re_{in}^{0.5})$ versus x^*. Results for three values of ΔT ($\Delta T = 10$, 20, and 50 K) and three values of Re_{in} for each value of ΔT ($Re_{in} = 500$, 1000 and 2000) are shown in this figure. For each ΔT, it is clear that the results for all three values of Re_{in} collapse fairly well when $(Nu_x/Re_{in}^{0.5})$ is used on the vertical axis. This is not an attempt at developing an accurate correlation; the objective here is only to demonstrate the approximate form of dependence between Nu_x and Re_{in} at fixed values of W_{in}, ΔT, and P_{in}.

4.1.5. Effect of P_{in}

Increasing P_{in} while maintaining W_{in} constant results in increasing the inlet saturation temperature of the mixture, T_{in}, with associated changes in the physical and thermodynamic properties. Therefore, if W_{in}, ΔT, and Re_{in} were held constant while varying P_{in}, the impact on the results will be mainly due to changes in the thermophysical properties. In order to assess this impact for steam–air, the effect of P_{in} was investigated at two values of W_{in} (0% and 20%); both corresponding to $Re_{in} = 2000$ and $\Delta T = 20$ K. Before examining these results, it would be interesting to discuss the expected effect of P_{in} on the properties and the anticipated impact of this property change on the condensation process. The property most affected by the pressure is the mixture density, whereby ρ_M increases (almost linearly) with P_{in}. If Re_{in} is held constant, then u_M will decrease with an increase in P_{in}. A decrease in u_M results in a decrease in the interfacial shear and consequently, an increase in the liquid film thickness. Thicker liquid films with fixed ΔT result in lower Nu_x and lower condensation rates.

The results in Figs. 6(a)–(c) confirm the trends predicted above. Fig. 6(a) shows that δ^* increases as P_{in} increases for $W_{in} = 0.2$. For pure steam, the film thickness near the entrance of the channel is higher for higher P_{in} and because of the reduced heat transfer, the condensation length is longer for higher P_{in}. The trend of decreasing heat transfer with increasing P_{in} is clearly evident in Fig. 6(c). This decrease in heat transfer also results in a decrease in the momentum component of the pressure gradient. Therefore, the algebraic value of the pressure gradient decreases with an increase in P_{in}, as clearly shown by the results in Fig. 6(b).

4.2. Results for R134a–air mixtures

For the vapor–gas combination of R134a–air, detailed results were obtained for three inlet pressures

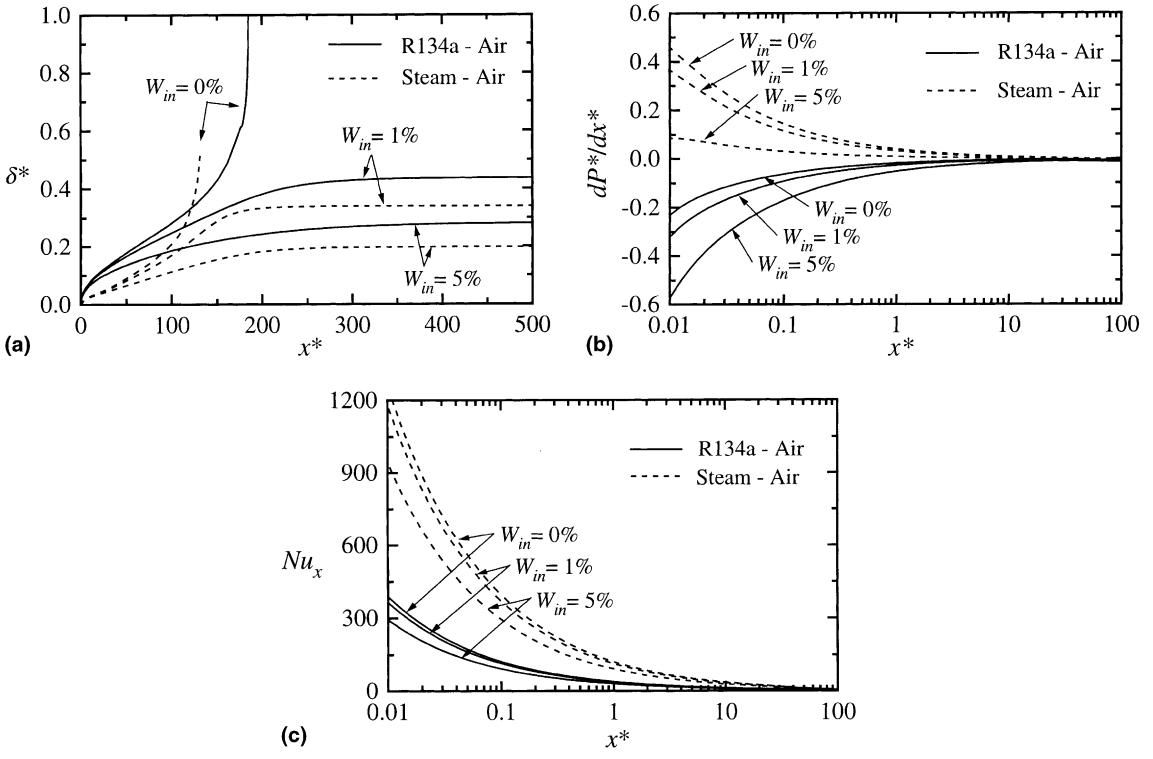

Fig. 7. Effect of W_{in} on the results of R134a–air at $P_{in} = 1$ atm, $Re_{in} = 1000$, and $\Delta T = 20$ K; (a) liquid film thickness; (b) pressure gradient; (c) local Nusselt number.

($P_{in} = 0.5$, 1, and 2 atm), three inlet Reynolds numbers ($Re_{in} = 500$, 1000, and 2000), a range of inlet gas concentrations ($0 \leqslant W_{in} \leqslant 0.2$), and a range of inlet-to-wall temperature differences ($5 \leqslant \Delta T \leqslant 50$ K). These results were found to have a common behavior exactly similar to the common behavior found in the steam–air results, discussed above in Section 4.1.1. Effects of the independent parameters W_{in}, ΔT, Re_{in}, and P_{in} on the condensation of R134a–air were also found to be similar to the effects of the independent parameters on the condensation of steam–air. The major difference between the R134a–air and steam–air results is in the properties, particularly ρ_M. For the same inlet conditions, ρ_M is higher for R134a–air than for steam–air. Therefore, based on the discussion in Section 4.1.5, thicker liquid films, lower heat transfer, and lower algebraic values of the pressure gradient are expected for R134a–air in comparison with steam–air at the same operating conditions. A sample of the R134a–air results is presented here including the variations of film thickness, pressure gradient, and local Nusselt number along the condensation path. Corresponding values for steam–air at the same conditions are shown in all the following figures for comparison.

The results for $P_{in} = 1$ atm, $Re_{in} = 1000$, $\Delta T = 20$ K, and $W_{in} = 0$ to 0.05 are shown in Figs. 7(a)–(c). These results confirm the thicker liquid films (Fig. 7(a)), the lower algebraic values of the pressure gradient (Fig. 7(b)), and the lower Nusselt numbers (Fig. 7(c)) for R134a–air compared with steam–air at the same conditions.

The effect of ΔT on δ^* is shown in Fig. 8 for $P_{in} = 1$ atm, $Re_{in} = 1000$, and $W_{in} = 0$ and 0.05. These results follow the same trend seen earlier in Fig. 4(a), and further confirm that the liquid films are thicker for R134a–air than steam–air. The effects of ΔT on (dP^*/dx^*) and Nu_x were found to follow the same trends seen earlier in Figs. 4(b) and (c) with lower values of (dP^*/dx^*) and Nu_x for R134a–air than steam–air.

Fig. 9 shows the effect of Re_{in} on Nu_x at $P_{in} = 1$ atm, $W_{in} = 0.05$, and $\Delta T = 10$ and 20 K. These results show that values of $(Nu_x Re_{in}^{-0.5})$ for $Re_{in} = 500$, 1000, and 2000 nearly collapse all along x^* for both values of ΔT. Again, Nu_x is lower for R134a–air than for steam–air at the same conditions.

The effect of pressure is shown in Fig. 10 with results for $Re_{in} = 2000$, $\Delta T = 20$ K, and $W_{in} = 0$ and 0.05. The trend in these results is similar to the trend seen earlier in Fig. 6(a) with thicker liquid films for R134a–air than for steam–air at the same conditions.

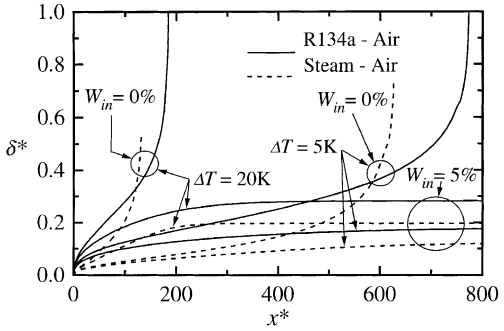

Fig. 8. Effect of ΔT on δ^* for R134a–air at $P_{in} = 1$ atm and $Re_{in} = 1000$.

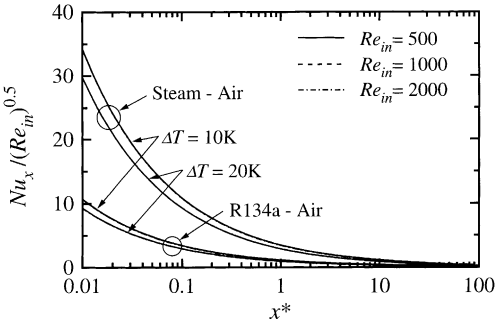

Fig. 9. Effect of Re_{in} on Nu_x for R134a–air at $P_{in} = 1$ atm and $W_{in} = 0.05$.

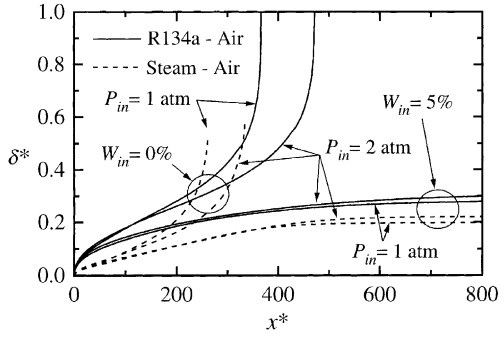

Fig. 10. Effect of P_{in} on δ^* for R134a–air at $Re_{in} = 2000$ and $\Delta T = 20$ K.

5. Concluding remarks

Detailed numerical results were obtained for laminar film condensation of two vapor–gas mixtures (steam–air and R134a–air) inside horizontal, parallel-plate channels. These results include local profiles of velocity u, temperature T, and gas concentration W, as well as axial variations of the liquid film thickness δ, pressure gradient (dP/dx), and Nusselt number Nu_x. For a specific vapor–gas combination, the solution requires four independent variables as input. These are the inlet pressure P_{in}, the inlet Reynolds number Re_{in}, the inlet gas con-

centration W_{in}, and the inlet-to-wall temperature difference ΔT. Wide ranges of these independent variables were covered and the influence of each variables on the condensation results was presented and discussed separately.

Because of the efficient numerical algorithm utilized here, it was possible to advance the solution from the inlet until complete condensation was achieved, except for the cases where flow reversal occurred along the condensation path. Flow reversal typically started at the top wall of the channel and it occurred only when the rate of condensation was high (conditions of high ΔT and low W_{in}).

The presence of gas was found to have significant effects on the condensation process. Values of δ, (dP/dx), and Nu_x decrease significantly as W_{in} increases. An analytical solution was developed for the liquid film thickness and velocity field at the end of the condensation path and it is demonstrated that the numerical solution converges to this analytical solution at large values of x.

In comparison to steam–air, R134a–air was found to produce larger δ, lower (dP/dx), and lower Nu_x at the same operating conditions. A major contributing factor to this trend is the high value of mixture density, which results in lower mixture velocity, lower interfacial shear, higher liquid film thickness, and lower condensation rate.

Acknowledgements

The financial support provided by the Natural Sciences and Engineering Research Council of Canada is gratefully acknowledged.

Appendix A. Exact solution for the flow conditions at the end of the condensation path

The geometry under consideration is shown in Fig. 1 and the flow situation is described in Section 1. The objective here is to develop an analytical solution for the flow parameters at the end of the condensation path. In this region, there is no heat transfer since the temperature across the condensate and the mixture layers is uniform at T_{wall} and the mixture consists of a gas fully saturated with vapor with a uniform gas concentration W_{ec}. The velocities ($u_{L,ec}$ and $u_{M,ec}$), temperature (T_{wall}), gas concentration (W_{ec}), film thickness (δ_{ec}), and pressure gradient $(dP/dx)_{ec}$ become independent of x. The densities of the liquid film and the mixture are constant and equal to ρ_L and ρ_M, respectively.

The momentum equations for the liquid and mixture regions in dimensionless form are, respectively,

$$\frac{d^2u^*_{L,ec}}{dy^{*2}} = \frac{1}{2}\left(\frac{\mu_{in}}{\mu_L}\right) Re_{in}\left(\frac{dP^*}{dx^*}\right)_{ec} \tag{A.1}$$

and

$$\frac{d^2u^*_{M,ec}}{dy^{*2}} = \frac{1}{2}\left(\frac{\mu_{in}}{\mu_M}\right) Re_{in}\left(\frac{dP^*}{dx^*}\right)_{ec}. \tag{A.2}$$

The boundary conditions for Eqs. (A.1) and (A.2) are: zero velocity at both walls, and equal velocity and shear stress at the interface. Integrating (A.1) and (A.2), we get the following velocity distributions:

$$u^*_{L,ec} = \frac{1}{4}\left(\frac{\mu_{in}}{\mu_L}\right)\left(\frac{dP^*}{dx^*}\right)_{ec} Re_{in}\left[y^{*2} + C_1y^* + C_2\right] \tag{A.3}$$

and

$$u^*_{M,ec} = \frac{1}{4}\left(\frac{\mu_{in}}{\mu_M}\right)\left(\frac{dP^*}{dx^*}\right)_{ec} Re_{in}\left[y^{*2} + C_3y^* + C_4\right]. \tag{A.4}$$

Applying the boundary conditions and reducing, we get

$$C_1 = -\frac{1 + ((\mu_M/\mu_L) - 1)\delta^{*2}_{ec}}{1 + ((\mu_M/\mu_L) - 1)\delta^*_{ec}}, \tag{A.5}$$

$$C_2 = 0, \tag{A.6}$$

$$C_3 = C_1 \tag{A.7}$$

and

$$C_4 = \frac{1 + ((\mu_M/\mu_L) - 1)\delta^{*2}_{ec}}{1 + ((\mu_M/\mu_L) - 1)\delta^*_{ec}} - 1. \tag{A.8}$$

From simple mass balances, the liquid and mixture mass flow rates, respectively, can be formulated as

$$\dot{m}_{L,ec} = \dot{m}_{in}\left(1 - \frac{W_{in}}{W_{ec}}\right) = \rho_L \int_0^{\delta_{ec}} u_{L,ec}\, dy \tag{A.9}$$

and

$$\dot{m}_{M,ec} = \dot{m}_{in}\left(\frac{W_{in}}{W_{ec}}\right) = \rho_M \int_{\delta_{ec}}^{H} u_{M,ec}\, dy. \tag{A.10}$$

In dimensionless form, Eqs. (A.9) and (A.10) reduce to

$$\int_0^{\delta^*_{ec}} u^*_{L,ec}\, dy^* = \left(\frac{\rho_{in}}{\rho_L}\right)\left(1 - \frac{W_{in}}{W_{ec}}\right) \tag{A.11}$$

and

$$\int_{\delta^*_{ec}}^{1} u^*_{M,ec}\, dy^* = \left(\frac{\rho_{in}}{\rho_M}\right)\left(\frac{W_{in}}{W_{ec}}\right). \tag{A.12}$$

Substituting from Eq. (A.3) into Eq. (A.11) and from Eq. (A.4) into Eq. (A.12) using the value of the coefficients given in Eqs. (A.5)–(A.8), we get the following two relations:

$$Re_{in}\left(\frac{dP^*}{dx^*}\right)_{ec} = -\left\{24\left(\frac{\rho_{in}}{\rho_L}\right)\left(\frac{\mu_L}{\mu_{in}}\right)\left(1-\frac{W_{in}}{W_{ec}}\right) \times \left[1+\left(\frac{\mu_M}{\mu_L}-1\right)\delta^*_{ec}\right]\right\} \Bigg/ \left\{3\delta^{*2}_{ec}-2\delta^{*3}_{ec}+\left(\frac{\mu_M}{\mu_L}-1\right)\delta^{*4}_{ec}\right\} \quad (A.13)$$

and

$$Re_{in}\left(\frac{dP^*}{dx^*}\right)_{ec} = -\left\{24\left(\frac{\rho_{in}}{\rho_M}\right)\left(\frac{\mu_M}{\mu_{in}}\right)\left(\frac{W_{in}}{W_{ec}}\right) \times \left[1+\left(\frac{\mu_M}{\mu_L}-1\right)\delta^*_{ec}\right]\right\} \Bigg/ \left\{1-3\delta^{*2}_{ec}+2\delta^{*3}_{ec}+\left(\frac{\mu_M}{\mu_L}-1\right) \times \left(4\delta^*_{ec}-9\delta^{*2}_{ec}+6\delta^{*3}_{ec}-\delta^{*4}_{ec}\right)\right\}. \quad (A.14)$$

Equating the pressure gradient in Eqs. (A.13) and (A.14), we get

$$\left[3\delta^{*2}_{ec}-2\delta^{*3}_{ec}+\left(\frac{\mu_M}{\mu_L}-1\right)\delta^{*4}_{ec}\right] \Bigg/ \left[\left(1-3\delta^{*2}_{ec}+2\delta^{*3}_{ec}\right) + \left(\frac{\mu_M}{\mu_L}-1\right)\left(4\delta^*_{ec}-9\delta^{*2}_{ec}+6\delta^{*3}_{ec}-\delta^{*4}_{ec}\right)\right] = \left(\frac{\rho_M}{\rho_L}\right)\left(\frac{\mu_L}{\mu_M}\right)\left(\frac{W_{ec}}{W_{in}}-1\right). \quad (A.15)$$

Eq. (A.15) is a fourth order polynomial and it can be solved iteratively for the value of δ^*_{ec} that corresponds to given values of ρ_L, ρ_M, μ_L, μ_M, W_{in}, and W_{ec} (determined from thermodynamic relations). The value of δ^*_{ec} is independent of Re_{in}. However, the dimensionless pressure gradient $(dP^*/dx^*)_{ec}$, calculated from either (A.13) or (A.14), is dependent on Re_{in}. Both Eqs. (A.13) and (A.14) suggest that $(dP^*/dx^*)_{ec}$ decreases with increasing Re_{in}. However, by examining the definitions of P^* and Re_{in}, we can easily see that the dimensional pressure gradient $(dP/dx)_{ec}$ actually increases with increasing $\dot{m}_{in}$ or Re_{in}. Finally, the velocity profiles $u^*_{L,ec}$ and $u^*_{M,ec}$ can be determined from Eqs. (A.3)–(A.8).

References

[1] D. Butterworth, R.G. Sardesai, P. Griffith, A.E. Bergles, Condensation, in: Heat Exchanger Design Handbook, Hemisphere, Washington, DC, 1983, Chapter 2.6.

[2] P.J. Marto, Fundamentals of condensation, in: S. Kakac, A.E. Bergles, E.O. Fernandes (Eds.), Two-Phase Flow Heat Exchangers: Thermal-hydraulic Fundamentals and Design, Kluwer Academic Publishers, Dordrecht, 1988, pp. 221–291.

[3] J.G. Collier, J.R. Thome, in: Convective Boiling and Condensation, third ed., Oxford University Press, Inc., New York, 1996, pp. 430–487.

[4] J.W. Rose, Fundamentals of condensation heat transfer: Laminar film condensation, JSME 31 (3) (1988) 357–375.

[5] J.W. Rose, Condensation heat transfer, Heat Mass Transfer 35 (1999) 479–485.

[6] C.Y. Wang, C.J. Tu, Effects of non-condensable gas on laminar film condensation in a vertical tube, Int. J. Heat Mass Transfer 31 (1988) 2339–2345.

[7] S.M. Ghiaasiaan, B.K. Kamboj, S.I. Abdel-Khalik, Two-fluid modeling of condensation in the presence of noncondensables in two-phase channel flows, Nucl. Sci. Eng. 119 (1995) 1–17.

[8] H.A. Hasanein, M.S. Kazimi, M.W. Golay, Forced convection in-tube steam condensation in the presence of noncondensable gases, Int. J. Heat Mass Transfer 39 (1996) 2625–2639.

[9] R.Y. Yuann, V.E. Schrock, X.M. Chen, Numerical modeling of condensation from vapor–gas mixtures for forced down flow inside a tube, in: Proceedings of the 7th International Conference on Nuclear Reactor Thermal Hydraulics, Saratoga, Springs, 1995, pp. 377–401.

[10] A. Narain, Y. Kizilyalli, Pressure driven flow of pure vapor undergoing laminar film condensation between parallel plates, Int. J. Non-linear Mech. 26 (1991) 501–520.

[11] A. Narain, G. Yu, Q. Liu, Interfacial shear models and their required asymptotic form for annular/stratified film condensation flows in inclined channels and vertical pipes, Int. J. Heat Mass Transfer 40 (1997) 3559–3575.

[12] H. Louahlia, P.K. Panday, Etude de la condensation par convection forcee du R113, R152a et du R12 sur une plaque plane horizontale, J. Phys. III France 6 (1996) 873–892.

[13] H. Louahlia, P.K. Panday, Transfert thermique pour la condensation du R123, du R134a et de leurs melanges, en ecoulement force entre deux plaques planes horizontales-Etude numerique, Rev. Generale Thermique 35 (1996) 615–624.

[14] H. Louahlia, P.K. Panday, Condensation en film entre deux plaques planes verticales: Comparaison des performances thermiques du R134a et du R12, Can. J. Chem. Eng. 75 (1997) 704–710.

[15] V. Srzic, H.M. Soliman, S.J. Ormiston, Analysis of laminar mixed-convection condensation on isothermal plates using full boundary-layer equations: mixtures of a vapor and a lighter gas, Int. J. Heat Mass Transfer 42 (1999) 685–695.

[16] G.J. Van Wylen, R.E. Sonntag, C. Borgnakke, Fundamentals of Classical Thermodynamics, fourth ed., Wiley, New York, 1994.

[17] Y.S. Chin, S.J. Ormiston, H.M. Soliman, A two-phase boundary-layer model for laminar mixed-convection condensation with a noncondensable gas on inclined plates, Heat Mass Transfer 34 (1998) 271–277.

[18] E.C. Siow, Numerical solution of a two-phase model for laminar film condensation of vapour–gas mixtures in channels, M.Sc. Thesis, University of Manitoba, Winnipeg, Manitoba, Canada, 2001.

[19] S.V. Patankar, Numerical Heat Transfer and Fluid Flow, Hemisphere, New York, 1980.

[20] Q. Lu, N.V. Suryanarayana, Condensation of a vapor flowing inside a horizontal rectangular duct, J. Heat Transfer 117 (1995) 418–424.

[21] W. Nusselt, Die oberflachenkondensation des wasserdampfes, Z. Detsch. Ing. 60 (1916) 541–546.